Toxic element-free Ti-based metallic glass ribbons with precious metal additions

Eray Yüce [a, b], Florian Spieckermann [b], Atacan Asci [a, b], Stefan Wurster [a],
Parthiban Ramasamy [a], Lixia Xi [c], Baran Sarac [a, *], Jürgen Eckert [a, b]

[a] Erich Schmid Institute of Materials Science, Austrian Academy of Sciences, Jahnstraße 12, A-8700, Leoben, Austria
[b] Department of Materials Science, Materials Physics, Montanuniversität Leoben, Jahnstraße 12, A-8700, Leoben, Austria
[c] Jiangsu Provincial Engineering Laboratory for Laser Additive Manufacturing of High-Performance Metallic Components, College of Materials Science and Technology, Nanjing University of Aeronautics and Astronautics, Yudao Street 29, Nanjing, 210016, China

ARTICLE INFO

ABSTRACT

We introduce four new biocompatible toxic element-free Ti-based metallic glass (MG) compositions with constant metalloid ($Si_{10}B_5$) and varying precious metal (PM) contents for simultaneous improvement in glass-forming ability (GFA) and corrosion properties. Being completely free from cytotoxic elements like Cu, Ni, or Be, which are indispensable for Ti-based bulk metallic glass production, limits the GFA of the studied alloys significantly. However, avoiding these elements also realizes an unprecedented corrosion resistance in simulated body fluids, which supports the potential utilization of the alloys as long-lasting dental implant material. The novel $Ti_{60}Zr_{15}Si_{10}B_5Pd_{10}$, $Ti_{60}Zr_{15}Si_{10}B_5Pt_{10}$, $Ti_{60}Zr_{15}Si_{10}B_5Pd_5Pt_5$, $Ti_{60}Zr_{15}Si_{10}B_5Pd_5Au_5$ alloys are obtained in ribbon form using conventional single-roller melt spinning. The effect of the PM additions on the GFA and corrosion resistance of the alloys is investigated comparatively with each other by synchrotron X-ray diffraction, differential scanning calorimetry, scanning electron microscopy, and cyclic polarization tests. Further, their Vickers hardness values are deduced using an ultra-sensitive micro indentation method, and the findings are discussed based on the composition dependence. It was found that the $Ti_{60}Zr_{15}Si_{10}B_5Pd_5Pt_5$ alloy presents a promising GFA while showing outstanding corrosion resistance in a simulated body fluid at 310 K.

1. Introduction

Titanium (e.g., commercial pure Ti) and its alloys (e.g., Ti−6Al−4V, Ti−6Al−7Nb, Ti−5Al−2.5Fe) are still the most commonly used implant materials in medical surgeries [1−3]. This stems from their inherently high corrosion resistance, good biocompatibility, and favorable mechanical properties [1,3−8]. Yet, some serious problems, such as their higher Young's modulus (110−120 GPa) compared to human bone (~30 GPa), the release of toxic metallic ions and/or particles through corrosion (insufficient chemical stability in the human body) remain to be solved [1,3,9,10]. In this regard, many efforts have focused on the development of new polycrystalline titanium alloys with improved biological and biomechanical properties. Particularly β-type Ti-alloys (e.g., Ti−35Nb−4Sn, Ti−34Nb−25Zr, Ti−29Nb−13Ta−4.6Zr)

containing only vital elements [1,11] have gathered great interest, owing to their reduced Young's modulus (40−60 GPa) and self-evident biological safety [3,12]. However, processing difficulties have restrained their usefulness for dental implants.

Meanwhile, Ti-based bulk metallic glasses (BMGs) were also considered as candidate materials for medical implants due to their better mechanical properties, such as higher strength and lower Young's modulus (2 GPa and 90 GPa, respectively), compared to Ti−6Al−4V (0.97 GPa and 115 GPa, respectively) [13,14]. It should be mentioned that no Ti-based BMG alloys without Ni, Be or Cu [13] are available until today. This stems from the fact that those alloy systems exhibit deep eutectics, which generally favor a high GFA. In such systems, the liquid state remains thermodynamically stable down to lower temperatures. In other words, the energy difference between the ordered and disordered states is very small at the eutectic composition, and this results in a lower driving force for the nucleation and growth of the crystalline phases [15]. As a matter of fact, it becomes easier to obtain a glassy structure in

bigger dimensions, which enables BMG production. It is well-known that Cu, Ni, and Be exhibit deep eutectics with Ti in their binary phase diagrams [16], and for this reason, they become indispensable if one strictly aims for a high GFA in order to produce Ti-based BMGs. Accordingly, the largest critical diameter has been reported to be over 50 mm for the $Ti_{32.8}Zr_{30.2}Ni_{5.3}Cu_9Be_{22.7}$ and $Ti_{32.8}Zr_{30.2}Cu_9Fe_{5.3}Be_{22.7}$ BMG alloys [17,18].

Cu has been regarded for a long time as a highly cytotoxic element, and it should be completely discarded from biocompatible materials, which are essentially designed for long-term medical implant applications [1,9,12,19–23]. This stems from the fact that Cu imposes the risk of an inflammatory reaction when released into the body fluids, and even an ion release down to 250 ppm can lead to cytotoxicity effects [24]. This risk becomes quite pronounced for implants with continuous contact with the body fluids under substantial load. Harmful Cu ion release was also observed for $Ti_{40}Zr_{10}Cu_{36}Pd_{14}$ BMG, emphasizing that the amorphous structure of the alloy cannot mitigate the risk [25]. Moreover, alloying with Cu in order to realize lower cooling rates for BMG production jeopardizes the pitting corrosion resistance by destabilizing the passive oxide layer, leading to its rupture [1,26–29]. For instance, $Ti_{40}Zr_{10}Cu_{36}Pd_{14}$ BMG shows an inferior pitting corrosion resistance in saline solution (0.9 wt% NaCl) as pitting occurs around 500 mV/SCE, while the Ti–6Al–4V alloy exceeds 1600 mV/SCE [30]. The same BMG exhibits similar values ($\sim$ 500 mV/SCE) in Hanks solution, whereas Ti–6Al–4V reaches to more than 1000 mV/SCE. Further, $Ti_{45}Zr_{10}Cu_{31}Pd_{10}Sn_4$ BMG shows in Hanks' solution about 500 mV/SCE for the initiation of pitting [31,32]. The same BMG depicts $\sim$ 600 mV/Ag/AgCl in 1 wt% lactic acid and PBS aqueous solutions [33]. This is a serious drawback since it undermines the potential application of the alloy as a medical implant, leaving its better mechanical properties as the sole advantage over conventional crystalline alloys. Nevertheless, all Ti-based BMGs reported in the literature contain Ni, Cu, or Be. Therefore, it is crucial to find new glass-forming alloys without any toxic elements for the efficient utilization of Ti-based metallic glasses in implant materials. Obviously, there has to be a compromise between the GFA and the biocompatibility/electrochemical stability of the alloy.

In this regard, there have been very few reports on truly biocompatible Ti-based MGs, where all the alloy constituents are specifically chosen from only biocompatible elements [1,11,34]. Until today $Ti_{60}Zr_{10}Ta_{15}Si_{15}$ in ($Ti_xZr_yTa_z)_{85}Si_{15}$ and $Ti_{45}Zr_{10}Pd_{40}Si_5$ in $Ti_{45}Zr_{50-x}Pd_xSi_5$ systems [10,35]; $Ti_{60}Nb_{15}Zr_{10}Si_{15}$ [1]; $Ti_{42}Zr_{40}$-Ta_3Si_{15} in the ($Ti_xZr_yTa_z)_{85}Si_{15}$ system [4,9,29,36,37]; $Ti_{42}Zr_{40}Sn_3Si_{15}$ and $Ti_{42}Zr_{40}Sn_3Si_{10}Ge_5$ [37]; $Ti_{20}Zr_{20}Nb_{20}Hf_{20}Si_{20}$ and $Ti_{30}Zr_{25}Nb_{25}Si_{15}Ga_3B_2$ MG alloys have been reported. Except for the $Ti_{20}Zr_{20}Nb_{20}Hf_{20}Si_{20}$ and $Ti_{30}Zr_{25}Nb_{25}Si_{15}Ga_3B_2$ MG alloys, which are based on a high-entropy alloy design approach and thus contain less titanium, all the reported Ti-based MG alloys can be classified under TM-M (Transition metal − Metalloid) type metallic glasses.

In such systems, the glass-forming alloys generally consist of 75−85 at.% transition metals and 15−25 at.% metalloids [15]. They commonly feature a deep eutectic around compositions of 15−25 at.% metalloids [15]. The TM and M contents of the alloy can also be a mixture of different kinds of elements. The main purpose of the metalloids is to lower the liquidus temperature (T_{liq}) of titanium. Nevertheless, none of the biocompatible elements [1,11] render an effective reduction in T_{liq} of Ti as Cu, Ni, or Be do. As a result, the achievable critical thickness of the amorphous structure remains very limited. In other words, the GFA of the alloy is marginal. This is the reason why all the above-mentioned truly biocompatible Ti-based MG alloys have been reported to be only in ribbon form. On the other hand, their pitting corrosion resistance and chemical stability are superior to any Ti-based BMG and polycrystalline Ti-based dental alloys. In this sense, the alloying

with different PM elements up to modest (10 at.%) atomic fractions may be worth the effort since these noble metals are biocompatible, and they might also improve the GFA of the alloys [1].

From the GFA point of view, the 3 precious metal elements Pd, Pt and Au have different merits. It is well-known that an alloy substituent should possess a large negative enthalpy of mixing with the main alloy constituents [38], in our case, with Ti. Since $\Delta H_{(Ti-Pt)}^{mix} = -73.698$ kJ/mol, $\Delta H_{(Ti-Pd)}^{mix} = -63.939$ kJ/mol and $\Delta H_{(Ti-Au)}^{mix} = -46.620$ kJ/mol at equiatomic compositions [39], all three elements are expected to improve the GFA. Regarding the atomic radii mismatch, $|r_{Pd} - r_{Ti}|/r_{Ti} = 0.059$, $|r_{Pt} - r_{Ti}|/r_{Ti} = 0.051$ and $|r_{Au} - r_{Ti}|/r_{Ti} = 0.013$ with titanium, which lies well below of the 0.12 threshold for a high GFA as suggested by Inoue [1,38]. On the other hand, they all decrease the T_{liq} (1943 K) of Ti, and the eutectic temperatures of Ti–Pd, Ti–Pt and Ti−Au are 1393 K, 1583 K and 1640 K, respectively [16]. From the aspect of GFA, one can refer to our recent study [34] to see why the remaining alloy constituents Zr, Si and B are chosen in our alloy design strategy.

In this study, we aim to develop new biocompatible Ti-based metallic glasses with excellent corrosion resistance and evaluate their GFA and mechanical properties. In this context, we present four new inherently biocompatible Ti-based MG compositions free of toxic elements, alloyed with PMs in varying atomic fractions, namely $Ti_{60}Zr_{15}Si_{10}B_5Pd_{10}$, $Ti_{60}Zr_{15}Si_{10}B_5Pt_{10}$, $Ti_{60}Zr_{15}Si_{10}B_5Pd_5Pt_5$ and $Ti_{60}Zr_{15}Si_{10}B_5Pd_5Au_5$, which can be synthesized in the form of amorphous ribbons.

2. Experimental procedures

2.1. Sample preparation

Master alloys with nominal compositions (at.%) $Ti_{60}Zr_{15}$-$Si_{10}B_5Pd_{10}$, $Ti_{60}Zr_{15}Si_{10}B_5Pt_{10}$, $Ti_{60}Zr_{15}Si_{10}B_5Pd_5Pt_5$, and $Ti_{60}Zr_{15}$-$Si_{10}B_5Pd_5Au_5$ were prepared by arc melting elemental Ti (99.99%), Zr (99.95%), Si (99.4%), B (99.4%), Pd (99.9%), Pt (99.9%) and Au (99.99%) under a Zr-gettered high-purity Ar (99.999%) atmosphere. The alloy ingots were flipped and remelted five times for homogenization. Melt spinning of the ribbons was performed under the high-purity Ar atmosphere after flushing the vacuum chamber of the melt spinner twice with Ar and going down to a vacuum level of $\sim 3.10^{-6}$ mbar. The velocity of the copper wheel was kept constant at 31.4 m/s (the first five quenchings) at an ejection temperature range of 100 K for each alloy, prior to the last quenching performed at 23.5 m/s. The initial melt spinning experiments conducted at 31.4 m/s wheel speed resulted in a ribbon thickness of $\sim 33 \pm 3$ μm for $Ti_{60}Zr_{15}Si_{10}B_5Pd_{10}$, $\sim 32 \pm 3$ μm for $Ti_{60}Zr_{15}Si_{10}B_5Pt_{10}$, $\sim 32 \pm 3$ μm for $Ti_{60}Zr_{15}Si_{10}B_5Pd_5Pt_5$, $\sim 32 \pm 2$ μm for $Ti_{60}Zr_{15}$-$Si_{10}B_5Pd_5Au_5$ and $\sim 32 \pm 2$ μm for $Ti_{60}Zr_{20}Si_8Ge_7B_3Sn_2$ alloys. At 23.5 m/s wheel speed performed experiments yielded a ribbon thickness of $\sim 45 \pm 2$ μm for $Ti_{60}Zr_{15}Si_{10}B_5Pd_5Pt_5$ and $\sim 43 \pm 3$ μm for $Ti_{60}Zr_{15}Si_{10}B_5Pd_{10}$. Finally, from a new master alloy of $Ti_{60}Zr_{15}$-$Si_{10}B_5Pd_5Pt_5$, a ribbon thickness of $\sim 51 \pm 4$ μm was obtained at 15.7 m/s wheel speed. The produced ribbons are quenched using quartz crucibles.

2.2. Structural, thermal, and electrochemical characterization

The as-spun ribbons were subjected to X-ray diffraction (XRD) analysis to ascertain their amorphous structure. These measurements were performed in reflection configuration (D2 phaser − Bruker) using Co-$K\alpha$ ($\lambda = 1.78897$ Å) radiation. A differential scanning calorimeter (DSC) was used to determine the glass transition (T_g) and crystallization (T_x) temperatures of the amorphous ribbons. The tests were conducted using a Netzsch DSC 404 F1

Pegasus device under high purity (99.999%) Ar atmosphere at constant heating and cooling rates of 20 K/min.

For electrochemical characterization, an aqueous Ar-aerated 0.9 wt% NaCl solution was used in this study. The electrochemical measurements were conducted in a three-electrode glass cell at 310 K using a Pt counter electrode (0.5 mm diameter) and a reference electrode of Ag(s)/AgCl(s) containing an ion-permeable porous glass junction with 3 M NaCl electrolyte that has a redox potential of $+0.195$ V (at room temperature) vs. a reference hydrogen electrode. As the working electrode, parts of the ribbons with an area of 1 ± 0.1 cm^2 were immersed into the electrolyte. The electrochemical measurements were performed with a Gamry Interface 1010 E Potentiostat/Galvanostat/ZRA. Before the electrochemical tests, open circuit potential (OCP) was applied for 3600 s to confirm the stabilization of the working electrode/electrolyte interface. Electrochemical impedance spectroscopy (EIS) studies were conducted at OCP at an AC amplitude of 10 mV recorded from 100,000 Hz to 0.01 Hz before the polarization study. Cyclic polarization was implemented at a scan rate of 1 mV s^{-1} for forward and reverse scans. The forward scan started from -0.3 V vs. OCP and stopped at $+1.5$ V vs. Ag/AgCl or when the current density reached 0.01 A cm^{-2}. The reverse scan rate was 1 mV s^{-1} and stopped at 0 V vs. OCP. At least three tests were performed for each composition and electrolyte for statistical information. The surface of the ribbons were analyzed by scanning electron microscopy (SEM, Tescan MAGNA) using a voltage of 20 kV.

2.3. Synchrotron XRD

In-situ synchrotron X-ray diffraction was performed at the P02.1 beamline of PETRA III at DESY, Hamburg using a Varex XRD 4343CT (150 × 150 μm^2 pixel size, 2880 × 2880 pixel area) detector with a photon energy of 60.0 keV in transmission setup. The beam size was 900 μm, and the sample-to-detector distance was 0.33 m. The diffraction patterns were carefully calibrated using an Al$_2$O$_3$ reference (NIST 674a), and the pyFAI software [40] was used for azimuthal integration. Full azimuthal integration was used to collect the integral geometric information about the sample.

2.4. Microhardness measurements

Vickers microhardness measurements of the as-spun ribbons were conducted with a microhardness tester (Zwick/Roell, EMCO-TEST DURASCAN) using a load of 25 mg and 10 s holding time. Nine tests were performed for each alloy composition for statistical purposes. For improved accuracy, the indents were examined by scanning electron microscopy (TESCAN MAGNA).

3. Results and discussion

3.1. Thermal properties

Fig. 1 Shows the continuous-heating DSC scans of the novel as-spun metallic glass ribbons along with the previously reported [34] Ti$_{60}$Zr$_{20}$Si$_8$Ge$_7$B$_3$Sn$_2$ alloy. A two-stage crystallization event is observed for all alloys. In order to verify whether the relatively small heat releases of Ti$_{60}$Zr$_{15}$Si$_{10}$B$_5$Pd$_{10}$ and Ti$_{60}$Zr$_{15}$Si$_{10}$B$_5$Pt$_{10}$ are actually stemming from the first stages of their crystallization behaviors, the isochronal DSC scans were performed for both alloys and the annealed samples were tested by XRD analysis. The results are depicted in Fig. S2. In general, the DSC scans of the alloys do not look much different from the Ti$_{60}$Zr$_{20}$Si$_8$Ge$_7$B$_3$Sn$_2$ alloy; however, they present distinctly separated exothermic peaks. The novel alloys with sole Pd or Pt additions show opposite characteristics. The Ti$_{60}$Zr$_{15}$Si$_{10}$B$_5$Pd$_{10}$ alloy has a clearly lower crystallization
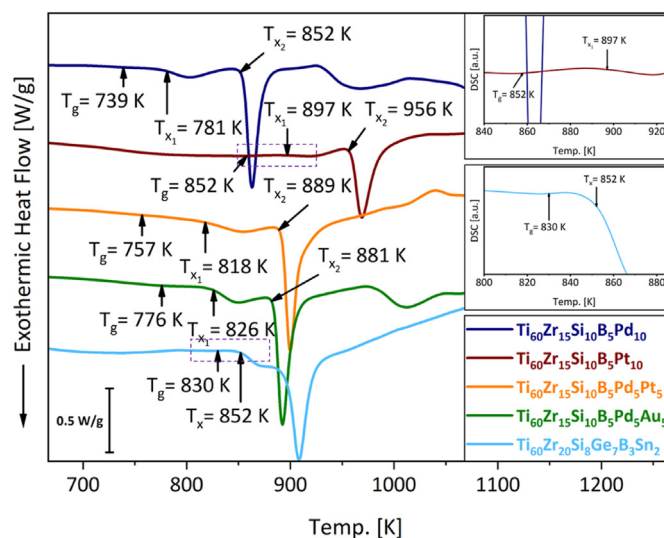
Fig. 1. High-temperature DSC scans of melt-spun amorphous ribbons recorded at a heating rate of 20 K/min and the glass transition temperatures (T_g), the crystallization onset temperatures (T_{x1} and T_{x2}) of the studied alloys. The insets represent the zoomed regions of the corresponding alloys (regions shown by dashed boxes).

temperature ($T_{x1} = 781 \pm 2$ K), and its peaks are located at lower temperatures, contrary to the crystallization behavior of Ti$_{60}$Zr$_{15}$Si$_{10}$B$_5$Pt$_{10}$. This difference might be related to the deeper eutectic temperature of Pd with Ti.

Conversely, upon sole Pt addition, $T_{x1} = 897 \pm 2$ K of Ti$_{60}$Zr$_{15}$Si$_{10}$B$_5$Pt$_{10}$ reaches the highest value of the studied alloys. As expected, $T_{x1} = 818 \pm 2$ K of the Ti$_{60}$Zr$_{15}$Si$_{10}$B$_5$Pd$_5$Pt$_5$ alloy is located between these two; however, the effect of Pd seems to be dominant, as this alloy still exhibits the second-lowest T_{x1} of the investigated alloys. For Ti$_{60}$Zr$_{15}$Si$_{10}$B$_5$Pd$_5$Au$_5$, $T_{x1} = 826 \pm 2$ K, which is slightly higher than that of Ti$_{60}$Zr$_{15}$Si$_{10}$B$_5$Pd$_5$Pt$_5$, might result from the higher eutectic temperature of Au with Ti. The glass transition temperatures (T_g) and the calculated extensions of the supercooled liquid regions (SCLR $= \Delta T_x = T_{x1} - T_g$) are presented in Table 1. It should be mentioned that because of the very noisy DSC signal at elevated temperatures, T_{liq} cannot be observed for the studied alloys. This results from the unavoidable reaction between the alloys and the crucible material of the DSC device [41]. Therefore, a commonly used important thermal indicator of the GFA, the reduced glass transition temperature ($T_{rg} = T_g/T_{liq}$) cannot be determined.

Table 1 reveals that the Ti$_{60}$Zr$_{15}$Si$_{10}$B$_5$Pd$_5$Pt$_5$ alloy yields the widest SCLR ($= \Delta T_x$), whereas the Ti$_{60}$Zr$_{20}$Si$_8$Ge$_7$B$_3$Sn$_2$ alloy without any PM addition presents a substantially narrower region. Moreover, all of the novel alloys appear to possess much wider SCLRs compared to the previously reported Ti$_{60}$Zr$_{20}$Si$_8$Ge$_7$B$_3$Sn$_2$ alloy. In general, this indicates an increased GFA [15,38]. However, none of the ascertained T_g values, which are determined with the

Table 1

Thermal properties ($\Delta T_x = T_{x1} - T_g$), T_g = glass transition temperature, T_{x1} = crystallization onset temperature, and ejection temperatures (T_{eject}) of the investigated alloys. The error limit of the DSC is about ± 2 K.

Alloy	T_g [K]	T_{x1} [K]	ΔT_x [K]	T_{eject} [K]
Ti$_{60}$Zr$_{15}$Si$_{10}$B$_5$Pd$_{10}$	739	781	42	1753
Ti$_{60}$Zr$_{15}$Si$_{10}$B$_5$Pt$_{10}$	852	897	45	1791
Ti$_{60}$Zr$_{15}$Si$_{10}$B$_5$Pd$_5$Pt$_5$	757	818	61	1808
Ti$_{60}$Zr$_{15}$Si$_{10}$B$_5$Pd$_5$Au$_5$	776	826	50	1833
Ti$_{60}$Zr$_{20}$Si$_8$Ge$_7$B$_3$Sn$_2$	830	852	22	1823

last endothermic bumps prior to the crystallization peaks, is sufficiently distinct to be observed with the naked eye, and they can only be detected using a thermal analysis software (determined T_g values of the remaining alloys are presented in Fig. S1.). Thus, rather than comparing the ΔT_x values of individual alloys, it is valid to state that there is an increasing trend in GFA upon PM addition.

Recently, Cai et al. [42] have shown that the conventional temperature window for the thermoplastic net-shaping (TPN) could be extended over T_{x1}, and the accompanying nano-crystallization does not undermine the mechanical properties and the chemical stability of the $Ti_{40}Zr_{10}Cu_{34}Pd_{14}Sn_2$ BMG-forming alloy. When the processing temperature is increased, the viscosity decreases, and the implementation of the micro-scaled hierarchical structures becomes feasible. Through the extended temperature window, along with T_g, also the first crystallization peak disappears from the DSC trace of the alloy, and this happens despite the relatively large ratio between the crystallization enthalpies of peak-1 and the sum of peak-2 and peak-3, which is 0.283. In this work, however, the ratios between the first and main (second) crystallization peaks lie well-below the value of 0.215 for $Ti_{60}Zr_{15}Si_{10}B_5Pd_{10}$, 0.131 for $Ti_{60}Zr_{15}Si_{10}B_5Pt_{10}$, 0.159 for $Ti_{60}Zr_{15}Si_{10}B_5Pd_5Pt_5$, and finally 0.157 for $Ti_{60}Zr_{15}Si_{10}B_5Pd_5Au_5$. Therefore, it can be expected that the nanocrystallization products of peak-1 would be even less relevant for the studied alloys, and this might provide a larger temperature interval for the planned consolidation and/or TPN of the amorphous ribbons in the future.
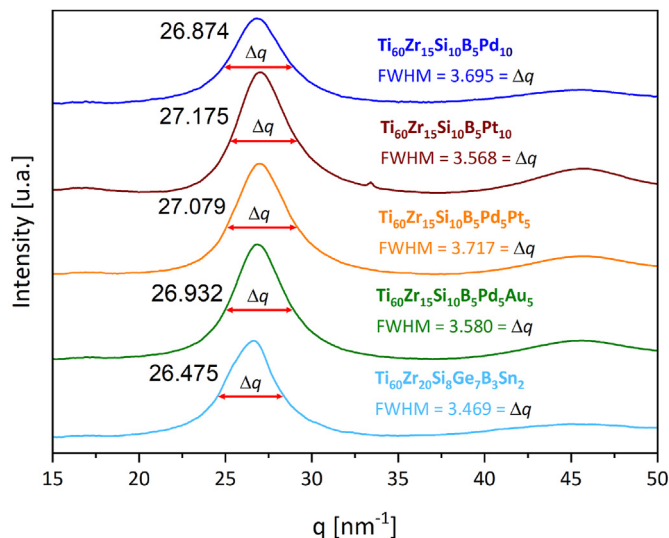
3.2. Structural properties

Fig. 2 depicts the obtained synchrotron XRD patterns of the as-spun ribbons. The patterns of the conventional X-ray diffraction in reflection configuration are also presented in Fig. S3. The numbers on the diffraction patterns show the scattering vector ($=q$) positions of the diffraction maxima of the corresponding alloys, revealing that these maxima shift to higher q values (or 2θ angles, because $q = 4\pi \times \sin\left(\frac{2\theta}{2}\right)/\lambda$, where λ is the X-ray wavelength) upon PM alloying. Since the position of the diffraction maximum is inversely related to the average radius of the first coordination shell [43,44], it can be stated that the average first neighbor atomic

Fig. 2. FWHM (Δq) values obtained from synchrotron XRD patterns. The magnitudes of Δq have been determined by applying a nonlinear Voigt fitting function to the synchrotron diffraction maxima of each alloy. The numbers on the left designate the q positions of the diffraction maxima of the corresponding alloys.

distance decreases upon alloying with PMs. While the new alloys contain more Si and B, the overall M fraction is reduced to 15 at.% at the expense of Ge atoms. Among M elements, Ge has the least atomic radius difference with Ti atoms, as $|r_{Ge} - r_{Ti}|/r_{Ti}$ is only 0.151, while $|r_{Si} - r_{Ti}|/r_{Ti} = 0.211$ and $|r_B - r_{Ti}|/r_{Ti} = 0.439$ [45]. Furthermore, $|r_{Zr} - r_{Ti}|/r_{Ti} = 0.096$, $|r_{Pd} - r_{Ti}|/r_{Ti} = 0.059$, $|r_{Pt} - r_{Ti}|/r_{Ti} = 0.051$ and $|r_{Au} - r_{Ti}|/r_{Ti} = 0.013$ [1]. Sn, on the other hand, yields $|r_{Sn} - r_{Ti}|/r_{Ti} = 0.081$ but it is excluded from the new alloy compositions. Namely, it can be stated that PM alloying was performed at the expense of Zr, Ge and Sn atoms.

According to these values, an overall decrease in the mean atomic bond length is not surprising since 5 at.% Zr (0.096), 7 at.% Ge (0.151) and 2 at.% Sn (0.081) are replaced with 2 at.% Si (0.211), 2 at.% B (0.439) and varying (10 at.%) PM (Pd = 0.059, Pt = 0.051, Au = 0.013) additions. Hence, for $Ti_{60}Zr_{15}Si_{10}B_5Pd_{10}$, $Ti_{60}Zr_{15}Si_{10}B_5Pt_{10}$ and $Ti_{60}Zr_{15}Si_{10}B_5Pd_5Pt_5$ alloys, a denser disordered atomic structure is achieved easily, as these alloy compositions maintain an increased atomic size distribution. Even for $Ti_{60}Zr_{15}Si_{10}B_5Pd_5Au_5$, whose atomic size distribution is slightly narrower than that for the $Ti_{60}Zr_{20}Si_8Ge_7B_3Sn_2$ alloy, the overall bond length appears to be shortened. This should be related to the absence of repelling atomic pairs, such as $\Delta H^{mix}_{(Sn-B)} = 17.78$ kJ/mol, $\Delta H^{mix}_{(Ge-B)} = 11.48$ kJ/mol and $\Delta H^{mix}_{(Sn-Si)} = 6.34$ kJ/mol (at equiatomic compositions) [39] in the alloys with PM substitutions.

The alloy with the densest atomic structure ($q = 27.175$ nm^{-1}) seems to be $Ti_{60}Zr_{15}Si_{10}B_5Pt_{10}$. This can be explained by the largest negative enthalpy of mixing between Ti–Pt and Zr–Pt atomic pairs ($\Delta H^{mix}_{(Ti_{60}-Pt_{10})} = -34.84$ kJ/mol; $\Delta H^{mix}_{(Zr_{15}-Pt_{10})} = -91.495$ kJ/mol) compared to those of Ti–Pd and Zr–Pd ($\Delta H^{mix}_{(Ti_{60}-Pd_{10})} = -30.074$ kJ/mol; $\Delta H^{mix}_{(Zr_{15}-Pd_{10})} = -83.355$ kJ/mol). Moreover, $|r_{Pt} - r_{Ti}|/r_{Ti} = 0.051$, which is the second-largest mismatch after $|r_{Pd} - r_{Ti}|/r_{Ti} = 0.059$. However, these assumptions do not hold for the $Ti_{60}Zr_{15}Si_{10}B_5Pd_{10}$ alloy, although it renders the second-largest negative mixing enthalpies and the widest atomic size distribution. Surprisingly, $Ti_{60}Zr_{15}Si_{10}B_5Pd_{10}$ is the least dense alloy among the PM-alloyed compositions. This points out that even upon alloying with two similar PM atoms, which results in large negative mixing enthalpies with other alloy constituents and shows roughly the same atomic radius mismatch, the resulting short-range order of the glassy structure is relatively different in the case of $Ti_{60}Zr_{15}Si_{10}B_5Pd_{10}$ and $Ti_{60}Zr_{15}Si_{10}B_5Pt_{10}$.

The second-densest alloy seems to be $Ti_{60}Zr_{15}Si_{10}B_5Pd_5Pt_5$. This composition also includes the PM atoms with relatively large ($\Delta H^{mix}_{(Ti_{60}-Pt_5)} = -20.073$ kJ/mol and $\Delta H^{mix}_{(Ti_{60}-Pd_5)} = -17.305$ kJ/mol; $\Delta H^{mix}_{(Zr_{15}-Pt_5)} = -68.626$ kJ/mol and $\Delta H^{mix}_{(Zr_{15}-Pd_5)} = -62.398$ kJ/mol) negative mixing enthalpies. Moreover, a wide atomic size distribution is realized through $|r_{Pd} - r_{Ti}|/r_{Ti} = 0.059$ and $|r_{Pt} - r_{Ti}|/r_{Ti} = 0.051$. Finally, when Pt and Pd are alloyed simultaneously, due to their positive enthalpy of mixing ($\Delta H^{mix}_{(Pt_5-Pd_5)} = 1.923$ kJ/mol), they repel each other. Therefore, besides its smaller negative heats with main alloy constituents, the introduction of a positive mixing enthalpy makes the $Ti_{60}Zr_{15}Si_{10}B_5Pd_5Pt_5$ less dense than the $Ti_{60}Zr_{15}Si_{10}B_5Pt_{10}$ alloy. As expected, the third-densest alloy is $Ti_{60}Zr_{15}Si_{10}B_5Pd_5Au_5$. Since $\Delta H^{mix}_{(Ti_{60}-Au_5)} = -13.102$ kJ/mol and $\Delta H^{mix}_{(Ti_{60}-Pd_5)} = -17.305$ kJ/mol and also $\Delta H^{mix}_{(Zr_{15}-Au_5)} = -51.346$ kJ/mol and $\Delta H^{mix}_{(Zr_{15}-Pd_5)} = -62.398$ kJ/mol are smaller than those of $Ti_{60}Zr_{15}Si_{10}B_5Pd_5Pt_5$, it is not surprising that $Ti_{60}Zr_{15}Si_{10}B_5Pd_5Au_5$ alloy renders a less densely packed atomic structure in comparison to $Ti_{60}Zr_{15}Si_{10}B_5Pd_5Pt_5$. Additionally, it also contains a repelling atomic pair of Pd–Au with $\Delta H^{mix}_{(Pd_5-Au_5)} = 0.116$ kJ/mol and a

narrower atomic size distribution of $|r_{Pd} - r_{Ti}|/r_{Ti} = 0.059$ and $|r_{Au} - r_{Ti}|/r_{Ti} = 0.013$ compared to those of $Ti_{60}Zr_{15}Si_{10}B_5Pd_5Pt_5$ with $|r_{Pd} - r_{Ti}|/r_{Ti} = 0.059$ and $|r_{Pt} - r_{Ti}|/r_{Ti} = 0.051$.

Recently, a simple but very effective $\Delta q - GFA$ correlation ($q = 4\pi \times \sin\left(\frac{2\theta}{2}\right)/\lambda$, where q is the scattering vector and λ is the X-ray wavelength) for individual ternary alloy libraries, was proposed by Li et al. [46]. They discovered a direct relation between the full-width at half-maximum (FWHM) of the first broad diffuse maximum (Δq) and the GFA of the alloy. In general, a broader diffuse maximum suggests better GFA and vice versa. This relation is so powerful that they even discovered two novel ternary BMGs using the data obtained from the sputtered metallic glass thin films. By evaluating the Δq values of the thin films, they reported two new BMG-forming alloys ($Zr_{43}Cu_{50}Cr_7$ and $Ir_{20}Co_{40}Ta_{40}$) and an improved critical diameter for the Zr−Cu−Al system. In this sense, we determined the FWHM values of the studied alloys to make a structural GFA comparison. The Δq magnitudes of the broad diffraction maxima were deduced from the synchrotron X-Ray diffraction patterns using a nonlinear Voigt fitting function. The magnitudes of Δq are presented in Fig. 2.

The Δq values reveal that the $Ti_{60}Zr_{15}Si_{10}B_5Pd_5Pt_5$ and $Ti_{60}Zr_{15}Si_{10}B_5Pd_{10}$ alloys have a distinctively higher GFA compared to the other ones, and the alloy with the lowest GFA is the composition without any PM additions. Additionally, the $Ti_{60}Zr_{15}Si_{10}B_5Pd_5Pt_5$ and $Ti_{60}Zr_{15}Si_{10}B_5Pd_{10}$ alloys are particularly easy to quench and yield the best results during the melt spinning process. That means the first five melt spinning experiments (at 31.4 m/s wheel velocity) conducted at different ejection temperatures (in a range of 100 K) generated amorphous ribbons. Moreover, for the $Ti_{60}Zr_{15}Si_{10}B_5Pd_5Pt_5$ alloy, it was possible to achieve an amorphous state at a lower copper wheel speed of 23.5 m/s from the same master alloy, again pointing out its improved GFA (See Fig. S4). On the other hand, the ribbon spun at 23.5 m/s for the $Ti_{60}Zr_{15}Si_{10}B_5Pd_{10}$ alloy yields an amorphous structure on its wheel-surface, while the free-surface turned up to be slightly crystallized. Later, an amorphous ribbon with a thickness of $\sim 51 \pm 4~\mu m$ (See Fig. S4) was successfully produced at 15.7 m/s wheel speed from a new master alloy of $Ti_{60}Zr_{15}Si_{10}B_5Pd_5Pt_5$.

Apparently, Pd atoms play a significant role in preserving the disordered structure, either as the sole PM source or mixed up with Pt or Au. On the other hand, compared to Pt, Pd atoms exhibit smaller negative mixing enthalpies with the other alloy constituents, except the slightly larger one with Si ($\Delta H^{mix}_{(Ti_{60} - Pt_{10})} = -34.84$ kJ/mol and $\Delta H^{mix}_{(Ti_{60} - Pt_5)} = -20.073$ kJ/mol; $\Delta H^{mix}_{(Ti_{60} - Pd_{10})} = -30.074$ kJ/mol and $\Delta H^{mix}_{(Ti_{60} - Pd_5)} = -17.305$ kJ/mol; $\Delta H^{mix}_{(Pt_{10} - B_5)} = -31.059$ kJ/mol and $\Delta H^{mix}_{(Pt_5 - B_5)} = -37.469$ kJ/mol; $\Delta H^{mix}_{(Pd_{10} - B_5)} = -27.718$ kJ/mol and $\Delta H^{mix}_{(Pd_5 - B_5)} = -33.365$ kJ/mol; $\Delta H^{mix}_{(Pt_5 - Si_{10})} = -43.644$ kJ/mol and $\Delta H^{mix}_{(Pt_{10} - Si_{10})} = -48,796$ kJ/mol; $\Delta H^{mix}_{(Pd_5 - Si_{10})} = -44.231$ kJ/mol and $\Delta H^{mix}_{(Pd_{10} - Si_{10})} = -49.576$ kJ/mol; $\Delta H^{mix}_{(Pt_5 - Zr_{15})} = -68.626$ kJ/mol and $\Delta H^{mix}_{(Pt_{10} - Zr_{15})} = -91.495$ kJ/mol; $\Delta H^{mix}_{(Pd_5 - Zr_{15})} = -62.398$ kJ/mol and $\Delta H^{mix}_{(Pd_{10} - Zr_{15})} = -83.355$ kJ/mol) [39].

Even though $Ti_{60}Zr_{15}Si_{10}B_5Pt_{10}$ renders the densest atomic structure (see Fig. 2), the largest negative heat of mixing between the alloy constituents do not promote the GFA since this alloy has the smallest Δq value among those with PM additions. This may result from the significantly higher melting temperature and heavier atomic weight of Pt compared to Pd. It should also be considered that Pd yields a more effective reduction in T_{liq} of Ti than Pt (the eutectic temperatures of Ti−Pd and Ti−Pt are 1393 K and 1583 K, respectively). This should contribute to the stabilization of the glass-forming liquid since alloying with Pd atoms lowers the

relative Gibbs free energy of the glass more than Pt atoms do [15]. Furthermore, the atomic size mismatch between Ti−Pd and Zr−Pd is larger than for Ti−Pt and Zr−Pt. Therefore, the lower GFA of $Ti_{60}Zr_{15}Si_{10}B_5Pt_{10}$ compared to $Ti_{60}Zr_{15}Si_{10}B_5Pd_{10}$ seems reasonable from thermodynamical and topological aspects.

The alloy with the highest GFA, namely $Ti_{60}Zr_{15}Si_{10}B_5Pd_5Pt_5$, possesses equal amounts of Pd and Pt, and according to the synchrotron XRD data, it has a slightly larger Δq than $Ti_{60}Zr_{15}Si_{10}B_5Pd_{10}$. Since $Ti_{60}Zr_{15}Si_{10}B_5Pt_{10}$ holds the lowest GFA among the alloys with PM additions, this result seems to contradict this at first glance. However, as mentioned before, alloying with Pt has its own merits, such as the largest negative heats with Ti, Zr and B. Besides, it increases the entropy of the alloy by making the crystallization more complex. On a broader scale, when PM atoms are alloyed simultaneously, the number of potentially repelling atomic pairs increases. For instance, the $Ti_{60}Zr_{15}Si_{10}B_5Pd_{10}$ and $Ti_{60}Zr_{15}Si_{10}B_5Pt_{10}$ alloys include only Si−B pairs with a slightly positive mixing enthalpy of 2.693 kJ/mol at a 0.666-mol fraction of Si. However, for the $Ti_{60}Zr_{15}Si_{10}B_5Pd_5Pt_5$ alloy, the number of potentially repelling atomic pairs increases to two, simply because of the Pd−Pt pair with $\Delta H^{mix}_{(Pd - Pt)} = 1.923$ kJ/mol at 0.5-mol fraction. This also explains its less densely packed atomic structure, even though it exhibits the highest GFA.

From this aspect, it makes sense that $Ti_{60}Zr_{15}Si_{10}B_5Pd_5Au_5$ shows even a lower packing density, owing to $\Delta H^{mix}_{(Au - Pd)} = 0.116$ kJ/mol at 0.5-mol fraction and also substantially smaller negative mixing enthalpies of Au with other components, which also explains its second-lowest GFA amongst the PM-alloyed compositions. In this sense, alloying with Au seems to have a clear disadvantage over Pd and Pt regarding its highest eutectic temperature and smaller negative mixing enthalpies with Ti, Zr, Si and B. Moreover, Au yields the smallest atomic radius mismatch with Ti [11], which is also undesired for a high GFA [38]. Indeed, during our melt spinning experiments, it was not possible to obtain a fully amorphous structure from the master alloys with the compositions of $Ti_{60}Zr_{15}Si_{10}B_5Au_{10}$ and $Ti_{60}Zr_{15}Si_{10}B_5Pt_5Au_5$.

To summarize, there is no direct correlation observed between the atomic packing density and the GFA. The alloys with sole PM addition ($Ti_{60}Zr_{15}Si_{10}B_5Pd_{10}$ and $Ti_{60}Zr_{15}Si_{10}B_5Pt_{10}$) are the loosest and the densest (latter) and Pd addition greatly promotes the GFA of the alloys. On the other hand, 10 at.% Pt alloying results in the lowest GFA of PM-alloyed compositions. Meanwhile, alloying with Pd does not result in a closely-packed atomic structure, unlike Pt, but it greatly enhances the GFA. Bearing in mind that $Ti_{60}Zr_{15}Si_{10}B_5Au_{10}$ and $Ti_{60}Zr_{15}Si_{10}B_5Pt_5Au_5$ amorphous alloys could not be obtained at all, and $Ti_{60}Zr_{15}Si_{10}B_5Pt_{10}$ yields the lowest GFA of the PM-alloyed compositions, the pronounced GFA of $Ti_{60}Zr_{10}Si_{10}B_5Pd_5Pt_5$ and $Ti_{60}Zr_{15}Si_{10}B_5Pd_{10}$ alloys and the achievement of $Ti_{60}Zr_{10}Si_{10}B_5Pd_5Au_5$ emphasizes the positive effect of Pd on the GFA.

3.3. Microhardness measurements

Representative SEM images of the conducted microindentation tests are presented in Fig. 3. The measured microhardness and estimated compressive yield strength ($\sigma_y = \frac{H_v \times g_0}{3}$, $g_0 = 9.81~m/s^2$) [47] values of the studied alloys are listed in Table 2. It is well-known that hardness and strength values are strongly dependent on alloy composition and are directly associated with the average atomic bond strength due to the lack of crystal defects in amorphous alloys [48]. Thus, it can be expected that the hardness should be related to T_g or elastic moduli, as these are also physical parameters determined by the atomic cohesive energy [15]. Indeed,
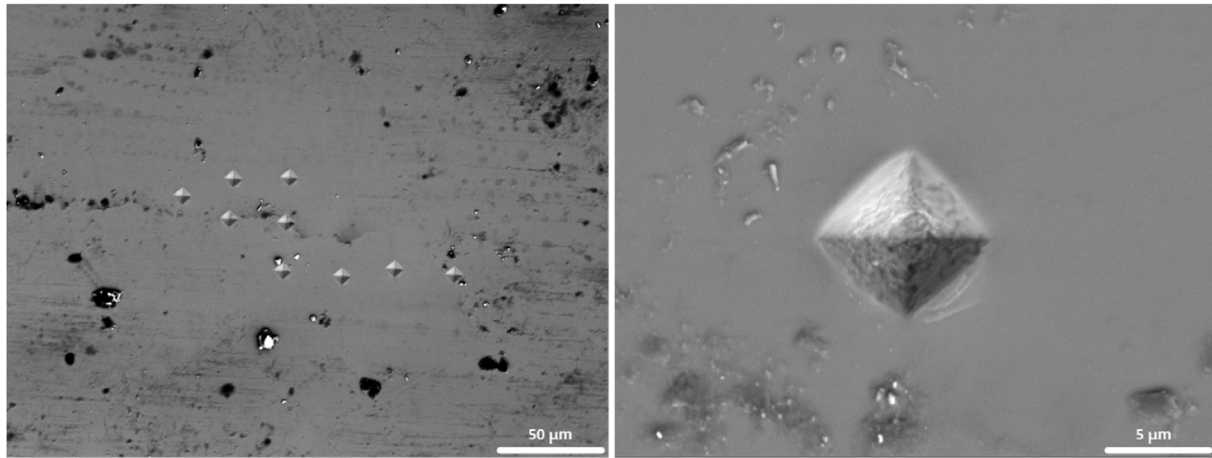
Fig. 3. Microindentation imprints on the as-spun $Ti_{60}Zr_{15}Si_{10}B_5Pd_{10}$ amorphous ribbon.

Table 2
Measured microhardness and estimated compressive yield strength ($\sigma_y = \frac{H_v \times g_0}{3}$, $g_0 = 9.81 \ m/s^2$) of the as-spun amorphous ribbons.

Alloy	Hardness [H_v]	σ_y [MPa]
$Ti_{60}Zr_{15}Si_{10}B_5Pd_{10}$	714 ± 8	2335 ± 26
$Ti_{60}Zr_{15}Si_{10}B_5Pt_{10}$	864 ± 14	2825 ± 46
$Ti_{60}Zr_{15}Si_{10}B_5Pd_5Pt_5$	766 ± 11	2505 ± 36
$Ti_{60}Zr_{15}Si_{10}B_5Pd_5Au_5$	816 ± 7	2668 ± 23
$Ti_{60}Zr_{20}Si_8Ge_7B_3Sn_2$	825 ± 11	2698 ± 36

the order of the microhardness test results coincides with the order of the deduced T_g values.

The hardest and the softest alloys are $Ti_{60}Zr_{15}Si_{10}B_5Pt_{10}$ and $Ti_{60}Zr_{15}Si_{10}B_5Pd_{10}$, respectively. Alloys with the highest GFA, namely $Ti_{60}Zr_{15}Si_{10}B_5Pd_{10}$ and $Ti_{60}Zr_{15}Si_{10}B_5Pd_5Pt_5$, are significantly softer than the others. Interestingly, the PM-alloys with the lowest GFA, i.e., $Ti_{60}Zr_{15}Si_{10}B_5Pt_{10}$ and $Ti_{60}Zr_{15}Si_{10}B_5Pd_5Au_5$, render substantially higher hardness values. The hardest alloy, $Ti_{60}Zr_{15}Si_{10}B_5Pt_{10}$, which also shows the densest atomic structure, is probably so hard due to its pronounced negative enthalpy of mixing values with the main alloy constituents of Ti, Zr and Si, which in turn points to the strongest bond strength.

However, this assumption does not hold for $Ti_{60}Zr_{15}Si_{10}B_5Pd_{10}$. This is the least dense alloy with considerably large negative heat of mixings, but it turns out to be the softest one as well. Considering that Pd has a lower bulk modulus and hardness compared to Pt, its introduction into the alloy might be the reason for the lowest hardness value of this composition. Another contributor might be the difference between the short-range order of $Ti_{60}Zr_{15}Si_{10}B_5Pd_{10}$ and $Ti_{60}Zr_{15}Si_{10}B_5Pt_{10}$. Both Pd and Pt preferably make bonds with Zr and Si, followed by B and Ti. Similarly, for Ti, the largest negative mixing enthalpies are again with Pd and Pt, followed by Si and B. That is, $Ti_{60}Zr_{15}Si_{10}B_5Pt_{10}$ and $Ti_{60}Zr_{15}Si_{10}B_5Pd_{10}$ do not differ by means of their bonding preference. Nevertheless, even though Pd and Pt are considered to be topologically equal in structural models, the differences in their electronic structure and also mixing enthalpies with the main alloy constituents lead to significant changes in atomic clusters [49]. For the $Ti_{60}Zr_{15}Si_{10}B_5Pd_{10}$ alloy, the lowest hardness may be related to a short-range order, in which the adjacent atomic clusters are connected via non-directional metallic bonds with high mobility. Concurrently, the atomic clusters in $Ti_{60}Zr_{15}Si_{10}B_5Pt_{10}$ should be connected through directional PM−Metalloid covalent bonds. For the second-softest $Ti_{60}Zr_{15}Si_{10}B_5Pd_5Pt_5$ alloy, the Vickers hardness value is relatively lower than that of $Ti_{60}Zr_{15}Si_{10}B_5Pt_{10}$, highlighting the strong softening effect of Pd, even when it is alloyed with Pt concomitantly.

For the $Ti_{60}Zr_{15}Si_{10}B_5Pd_5Au_5$ alloy, the Vickers-microhardness tests give interesting results. Even though this alloy contains softer Pd and the softest Au, it is moderately harder than $Ti_{60}Zr_{15}Si_{10}B_5Pd_{10}$ and $Ti_{60}Zr_{15}Si_{10}B_5Pd_5Pt_5$. Moreover, this alloy is the one with the lowest average bond strength, and it exhibits a loosely packed atomic structure. In other words, its structural properties are opposite to those of $Ti_{60}Zr_{15}Si_{10}B_5Pt_{10}$, yet together they are the hardest PM-alloys. This might be related to the smallest negative mixing enthalpies of Au with the other elements in the composition. Unlike Pt and Pd, whose bonding preferences follow the same order, Au cannot bind to Zr, since all of the Zr atoms would be already occupied by 10 at.% Si and 5 at.% Pd in $Ti_{60}Zr_{15}Si_{10}B_5Pd_5Au_5$. This probably has an impact on the short-range order of the alloy, which might even induce local segregation in the atomic structure. Still, the dependency of hardness on the alloy compositions is not clearly understood, and some results are controversial. Further structure investigations for clarifying the details of short- and medium-range order of the different alloys are underway, but this is beyond the scope of the present paper.

3.4. Corrosion properties

Fig. 4. (a) shows the polarization behavior of the developed PM-containing Ti-based MG ribbons. The corrosion current density, J_{corr}, the corrosion potential, E_{corr}, and the anodic, β_a, and cathodic, β_c, beta constants are determined by Tafel extrapolation and provided in Table 3. The smallest J_{corr} is attained with the Pd_5Pt_5 addition (1.02×10^{-8} A cm^{-2}), where this value is several times smaller than for the other investigated alloy compositions. The theoretical density, ρ, and equivalent weight, EW, of the considered alloys are calculated using the equations in Ref. [50]. The average annual corrosion rate (ACR) of the samples is calculated using Eq. (1). And the results are presented in Table 3:

$$ACR = \frac{3.27 \times J_{corr} \times EW}{\rho} \quad (1)$$

The $Ti_{60}Zr_{15}Si_{10}B_5Pd_5Pt_5$ alloy exhibits the smallest ACR of $0.141 \pm 0.005 \ \mu m \ yr^{-1}$, which is several times smaller compared to that of the Pd_{10}-and Pt_{10}-bearing counterparts. On the other hand, $Ti_{60}Zr_{15}Si_{10}B_5Pd_5Au_5$ shows the highest corrosion rate (followed by $Ti_{60}Zr_{15}Si_{10}B_5Pd_{10}$), which results in inhomogeneous and micro-scale pitting on the surfaces of the alloys. As depicted by SEM
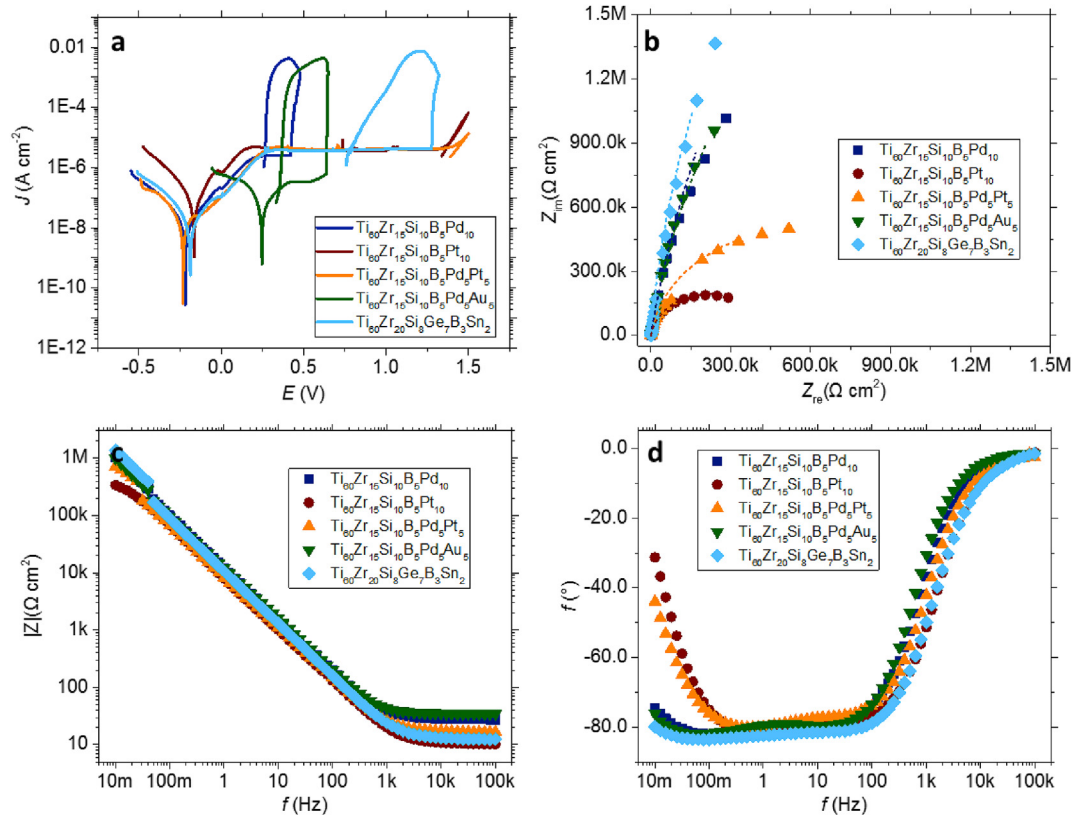
Fig. 4. (a) Forward potentiodynamic polarization scans of the Ti-based MG ribbons at a scan rate of 1 mV s^{-1}. The potential is given vs. Ag/AgCl reference electrode. (b) Nyquist, (c) Bode magnitude and (d) Bode phase plots of the examined compositions at their open-circuit potentials. All the tests were performed in 0.9 wt% NaCl solution at 37 °C. The measured data was simulated by R(QR) circuit, and the simulation results are depicted by short dash lines in (b).

Table 3
Corrosion properties of different Ti-based MG compositions. ρ: theoretical density, *EW*: equivalent weight, J_{corr}: corrosion current density, E_{corr}: corrosion potential, β_a: anodic beta constant, β_c: cathodic beta constant, *ACR*: annual corrosion rate.

| Composition	ρ [g cm^{-3}]	EW	J_{corr} [A cm^{-2}]	E_{corr} [V vs Ag/AgCl]	β_a	β_c	ACR [μm yr^{-1}]
Ti$_{60}$Zr$_{15}$Si$_{10}$B$_5$Pd$_{10}$	5.22	22.11	1.97×10^{-8}	−0.217	0.203	0.207	0.273
Ti$_{60}$Zr$_{15}$Si$_{10}$B$_5$Pt$_{10}$	6.027	25.59	3.35×10^{-8}	−0.165	0.527	0.331	0.465
Ti$_{60}$Zr$_{15}$Si$_{10}$B$_5$Pd$_5$Pt$_5$	5.624	23.85	1.02×10^{-8}	−0.230	0.130	0.085	0.141
Ti$_{60}$Zr$_{15}$Si$_{10}$B$_5$Pd$_5$Au$_5$	5.604	23.43	1.04×10^{-7}	−0.246	0.332	0.177	1.422
Ti$_{60}$Zr$_{20}$Si$_8$Ge$_7$B$_3$Sn$_2$	4.927	20.57	1.85×10^{-8}	−0.188	0.196	0.161	0.253

images in Fig. 5. (a) and (b), the apparent pitting corrosion related damage is much larger for Ti$_{60}$Zr$_{15}$Si$_{10}$B$_5$Pd$_5$Au$_5$ compared to Ti$_{60}$Zr$_{15}$Si$_{10}$B$_5$Pd$_{10}$, in accordance with the difference in their ACR.

The electrochemical impedance spectroscopy measurements recorded before the polarization tests at open circuit potential corroborate that incorporation of Pt can enhance the metal-electron interactions, as deduced from the relatively smaller semicircles in the Nyquist plot (Fig. 4 (b)) and the lowest |Z| in the whole frequency range (down to ∼ 10 Ω cm^2 at 100 kHz, Fig. 4 (c)) in the Bode magnitude plot. The EIS plots were fitted by a suitable R(QR) circuit, where the simulation results represented by short dashed lines in Fig. 4 (b) show a good match with the experimental data for all the samples.

The Bode phase plot in Fig. 4 (d) delineates an interesting drop in the Pd$_5$Pt$_5$-bearing sample at the mid-frequency range (1−100 Hz), indicating a relatively less-capacitive behavior and a high potential of metal-ion interactions in the beginning [51]. Hence, the larger and more stable passive oxide layer can be accounted for by the higher electron and ion interactions of the

samples with active Pd$_5$Pt$_5$-and Pt$_{10}$-bearing surfaces.

The EIS data presented in Fig. 4b−d is fitted by the most suitable equivalent circuit model, R(QR), with acceptable chi-squared values and parameter errors (Table 5). The solution resistance R_s ranges between 10.3 and 34.53, marginally influencing the overall results. The double-layer capacitance parameter *Y* of the constant-phase element (CPE) is slightly higher for Pt$_{10}$ and Pd$_5$Pt$_5$ containing alloys which can be related to the higher ionic accumulation, which also enhances the electron transfer as understood from the decrease in charge-transfer resistance *R*. The double-layer capacitance exponent *n* of the CPE is higher than 0.9, confirming the reliability of fitting [52]. A direct correlation between the CPEs and C_{dl} are provided in Ref. [53]. The ion and electron interactions between the samples and electrolytes are highly correlated with the surface composition. Our X-ray photoelectron spectroscopy investigation with a representative Ti$_{60}$Zr$_{15}$Si$_{10}$B$_5$Pd$_{10}$ sample shows that there are significant amounts of oxides, i.e., TiO$_2$, ZrO$_2$ and PdO with a possibility of C−O, C−OH and Si−O interactions provided in Table 6. Similarly, the other samples are expected to form oxides of
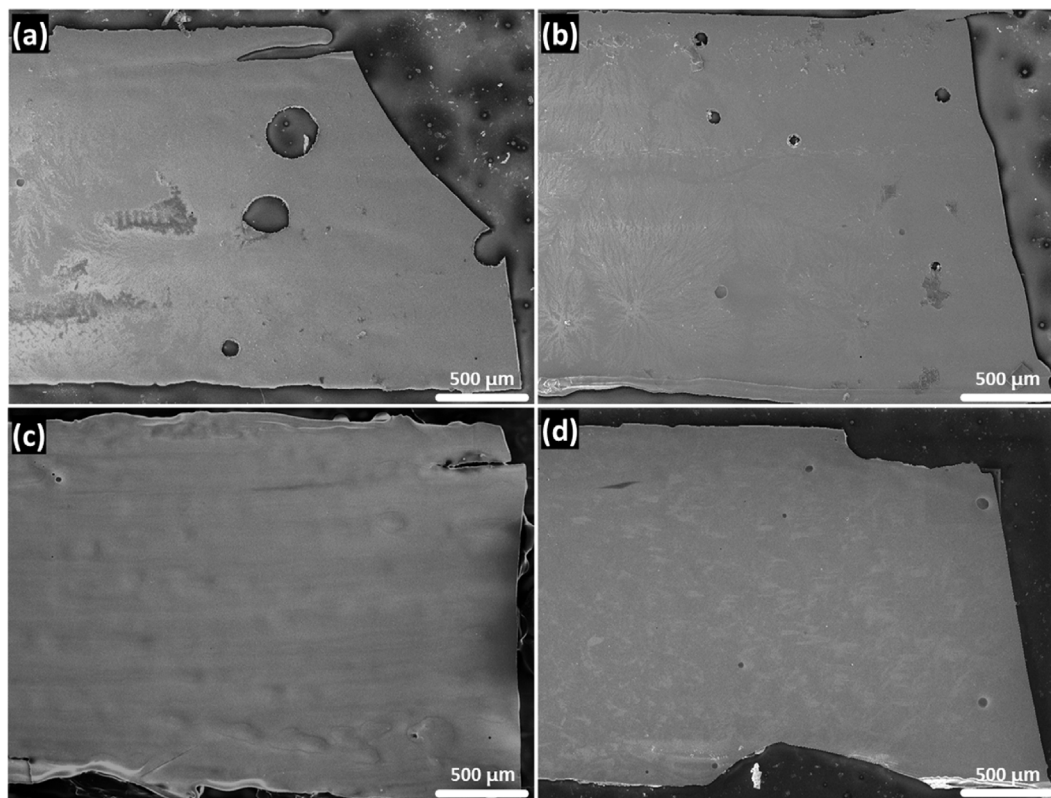
Fig. 5. SEM micrographs of the (a) $Ti_{60}Zr_{15}Si_{10}B_5Pd_5Au_5$, (b) $Ti_{60}Zr_{15}Si_{10}B_5Pd_{10}$, (c) $Ti_{60}Zr_{15}Si_{10}B_5Pt_{10}$ and (d) $Ti_{60}Zr_{15}Si_{10}B_5Pd_5Pt_5$ amorphous ribbons obtained after the polarization tests. The alloys with the low corrosion resistance, $Ti_{60}Zr_{15}Si_{10}B_5Pd_5Au_5$ and $Ti_{60}Zr_{15}Si_{10}B_5Pd_{10}$ exhibit micro-scale pitting (**a–b**), while the apparent pitting damage on $Ti_{60}Zr_{15}Si_{10}B_5Pd_{10}$ is considerably smaller. Concurrently, both $Ti_{60}Zr_{15}Si_{10}B_5Pt_{10}$ and $Ti_{60}Zr_{15}Si_{10}B_5Pd_5Pt_5$ show no pitting event (**c–d**) after the polarization tests.
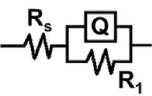
Table 4
Passivation and pitting corrosion of different Ti-based MG compositions. J_{pass}: passivation current density, E_{pit}: pitting potential, E_{rp}: repassivation potential, η_{pit}: passivation domain, ζ_{rp}: repassivation domain.

Composition	J_{pass} [A cm^{-2}]	E_{pit} [V vs Ag/AgCl]	E_{rp} [V vs Ag/AgCl]	η_{pit} (V) [$E_{pit} - E_{corr}$]	ζ_{rp} (V) [$E_{rp} - E_{corr}$]
$Ti_{60}Zr_{15}Si_{10}B_5Pd_{10}$	2.52×10^{-6}	0.422	0.266	0.639	0.483
$Ti_{60}Zr_{15}Si_{10}B_5Pt_{10}$	4.84×10^{-6}	1.358	1.392	1.523	1.557
$Ti_{60}Zr_{15}Si_{10}B_5Pd_5Pt_5$	4.77×10^{-6}	1.406	1.435	1.582	1.611
$Ti_{60}Zr_{15}Si_{10}B_5Pd_5Au_5$	3.39×10^{-7}	0.639	0.353	0.393	0.107
$Ti_{60}Zr_{20}Si_8Ge_7B_3Sn_2$	3.92×10^{-6}	1.277	0.787	1.465	0.975

Table 5
Fitting of the EIS data by R_s (Q_1R_1) equivalent circuit model. R_s: solution resistance, Y: double-layer capacitance parameter of CPE, n: double-layer capacitance exponent of CPE, R: charge-transfer resistance, χ^2: chi-squared. The error percentages for individual parameters are shown in parentheses.

	$Ti_{60}Zr_{15}Si_{10}B_5Pd_{10}$	$Ti_{60}Zr_{15}Si_{10}B_5Pt_{10}$	$Ti_{60}Zr_{15}Si_{10}B_5Pd_5Pt_5$	$Ti_{60}Zr_{15}Si_{10}B_5Pd_5Au_5$	$Ti_{60}Zr_{20}Si_8Ge_7B_3Sn_2$
R_s (Ω cm^2)	27.76 (%1.6)	10.3 (%0.9)	17.06 (%3.7)	34.53 (%1.5)	13.02 (%3.85)
Y (Ss^{n}cm^{-2})	1.392×10^{-5} (%1.4)	2.228×10^{-5} (%0.8)	1.875×10^{-5} (%3.1)	1.439×10^{-5} (%1.3)	1.327×10^{-5} (%3)
n (−)	0.9231 (%0.3)	0.9111 (%0.2)	0.9222 (%0.7)	0.9177 (%0.3)	0.9606 (%0.7)
R (Ω cm^2)	8.613×10^6 (%42.3)	4.506×10^5 (%2.6)	1.131×10^6 (%0.7)	1.319×10^7 (%62.6)	1.229×10^7 (%117)
χ^2	5.417×10^{-3}	1.446×10^{-3}	2.637×10^{-2}	4.63×10^{-3}	2.765×10^{-2}

precious metals and Sn included in that composition.

The $Ti_{60}Zr_{20}Si_8Ge_7B_3Sn_2$ alloy, which was previously subjected to electrochemical tests with the same solution at room temperature [34] and used for comparison purposes in this study, also shows inferior corrosion resistance as compared to the $Ti_{60}Zr_{15}Si_{10}B_5Pd_5Pt_5$ alloy. Simultaneous alloying of Pd and Pt was previously shown to enhance the stability of various nanostructures

using different electrochemical tests and electrolytes [54–58]. In this case, the co-existence of these two PMs creates a stable oxide layer, as revealed by the largest passivation η_{pit} and repassivation ζ_{rp} domain (Table 4). Furthermore, for the $Ti_{60}Zr_{15}Si_{10}B_5Pd_5Pt_5$ and $Ti_{60}Zr_{15}Si_{10}B_5Pt_{10}$ alloys, a rather smooth transition to the pitting region with a small current rise until 1.5 V takes place, indicating negligible pitting damages confirmed by the SEM images in Fig. 5.

Table 6
Surface composition analysis of the as-spun $Ti_{60}Zr_{15}Si_{10}B_5Pd_{10}$ sample by XPS.

Peak Name	at. %
O1s (TiO_2, ZrO_2, PdO)	32.2
O1s (C—O, C—OH, Si—O)	15.5
O1s (organic oxygen)	1.6
C1s (sp3)	14.9
C1s (C—O(H))	6.2
C1s (O—C—O)	3.8
C1s (carbide)	1.0
Ti2p3 (TiO_2)	12.7
Ti2p3 (metal)	3.0
Zr3d5 (ZrO_2)	4.2
Zr3d5 (metal)	0.6
Si2p3	3.4
Pd3d5 (carbide)	0.7
Pd3d5 (PdO)	0.2

(c) and (d). High magnification SEM imaging of the pitting corrosion related damage is presented in Fig. S5.

4. Conclusions

Four new PM-alloyed Ti-based MG compositions without any harmful elements are introduced. The GFA of the new truly biocompatible alloys was improved, and their disordered atomic structures became denser through the addition of PM constituents. The FWHM values (Δq) of the amorphous diffraction maxima obtained from synchrotron XRD experiments reveal that the order of GFA, from the highest to lowest, is $Ti_{60}Zr_{15}Si_{10}B_5Pd_5Pt_5$, $Ti_{60}Zr_{15}Si_{10}B_5Pd_{10}$, $Ti_{60}Zr_{15}Si_{10}B_5Pd_5Au_5$, $Ti_{60}Zr_{15}Si_{10}B_5Pt_{10}$ and $Ti_{60}Zr_{20}Si_8Ge_7B_3Sn_2$. Apparently, Pd plays the most important role in stabilizing the amorphous structure. Pt realizes the densest atomic structure when alloyed individually, whereas Pd behaves in the opposite way. Moreover, again upon sole Pd or Pt alloying, the $Ti_{60}Zr_{15}Si_{10}B_5Pd_{10}$ alloy has the lowest hardness and the second-highest GFA, whereas the $Ti_{60}Zr_{15}Si_{10}B_5Pt_{10}$ alloy exhibits the highest hardness and the lowest GFA of the PM-alloyed compositions. Additionally, Pd was found to promote the GFA when it is simultaneously alloyed with Pt or Au.

From the aspect of corrosion resistance, Pt seems to be the best option for improving the chemical stability of the alloys, regardless of whether it is alloyed individually or together with Pd. On the other hand, if Pd is the sole PM addition, the alloys show average corrosion properties compared to the best ones. All alloys except $Ti_{60}Zr_{15}Si_{10}B_5Pd_5Au_5$ render better corrosion properties than the Ti-based BMGs tested in simulated body fluids. Considering the high Ti-content of the compositions and the higher corrosion resistance of $Ti_{60}Zr_{15}Si_{10}B_5Pd_{10}$, it can be stated that the addition of 5 at.% Au deteriorates the chemical stability of $Ti_{60}Zr_{15}Si_{10}B_5Pd_5Au_5$. On the other hand, the substitution of 5 at.% Pt for Pd enhances the corrosion properties of $Ti_{60}Zr_{15}Si_{10}B_5Pd_{10}$. XPS data show mainly TiO_2 and ZrO_2 with C—O, C—OH and Si—O bond formations on the surface upon production.

The alloy with the best GFA, namely $Ti_{60}Zr_{15}Si_{10}B_5Pd_5Pt_5$, features promising mechanical properties such as a microhardness of 766 ± 11 H_v, an estimated compressive yield strength of 2505 ± 36 MPa and it could be spun at lower cooling rates (lower wheel speeds). It also exhibits excellent corrosion properties, the highest pitting potential, the widest passive region of 1.582 ± 0.03 V, and the lowest annual corrosion rate of 0.141 ± 0.005 μm yr^{-1}. Accordingly, it exhibits no corrosion-related damage, and its surface remains intact after the potentiodynamic polarization tests. Moreover, it has the widest SCLR of 61 ± 2 K. Regarding its promising structural and electrochemical properties,

the $Ti_{60}Zr_{15}Si_{10}B_5Pd_5Pt_5$ alloy is envisaged as a suitable candidate for a permanent medical implant material in the future after fine-tuning the alloy composition and/or improving the production technique and conditions.

Credit author statement

E. Yüce: Conceptualization, Investigation, Visualization, Formal analysis, Validation, Writing - Original Draft. **F. Spieckermann:** Supervision, Visualization, Formal analysis, Validation, Writing - Review & Editing. **A. Asci:** Writing - Review & Editing. **S. Wurster:** Writing - Review & Editing. **P. Ramasamy:** Supervision, Writing - Review & Editing. **L. Xi:** Writing - Review & Editing. **B. Sarac:** Conceptualization, Supervision, Formal analysis, Validation, Writing - Review & Editing, Funding acquisition. **J. Eckert**: Supervision, Writing - Review & Editing, Funding acquisition.

Declaration of competing interest

The authors declare that they have no known competing financial interests or personal relationships that could have appeared to influence the work reported in this paper.

Data availability

Data will be made available on request.

Acknowledgments

Appendix A. Supplementary data

Supplementary data to this article can be found online at https://doi.org/10.1016/j.mtadv.2023.100392.

References

[1] M. Calin, A. Gebert, A.C. Ghinea, P.F. Gostin, S. Abdi, C. Mickel, J. Eckert, Designing biocompatible Ti-based metallic glasses for implant applications, Mater. Sci. Eng. C Mater. Biol. Appl. 33 (2013) 875—883, https://doi.org/10.1016/j.msec.2012.11.015.

[2] M. Long, H. Rack, Titanium alloys in total joint replacement—a materials science perspective, Biomaterials 19 (1998) 1621—1639, https://doi.org/10.1016/S0142-9612(97)00146-4.

[3] M. Özcan, C. Hämmerle, Titanium as a reconstruction and implant material in dentistry: advantages and pitfalls, Materials 5 (2012) 1528—1545, https://doi.org/10.3390/ma5091528.

[4] Y.C. Liao, S.M. Song, T.H. Li, J.B. Li, P.H. Tsai, J. Jang, C.H. Huang, J.C. Huang, Y.S. Huang, C.H. Lin, Y.S. Lin, C.H. Chen, Synthesis and characterization of an open-pore toxic-element-free Ti-based bulk metallic glass foam for bio-implant application, J. Mater. Res. Technol. 9 (2020) 4518—4526, https://doi.org/10.1016/j.jmrt.2020.02.079.

[5] L. Bai, C. Cui, Q. Wang, S. Bu, Y. Qi, Ti—Zr—Fe—Si system amorphous alloys with excellent biocompatibility, J. Non-Cryst. Solids 354 (2008) 3935—3938, https://doi.org/10.1016/j.jnoncrysol.2008.05.015.

[6] S.P. Ong, W.D. Richards, A. Jain, G. Hautier, M. Kocher, S. Cholia, D. Gunter, V.L. Chevrier, K.A. Persson, G. Ceder, Python Materials Genomics (pymatgen): a robust, open-source python library for materials analysis, Comput. Mater.

Sci. 68 (2013) 314–319, https://doi.org/10.1016/j.commatsci.2012.10.028.

[7] B. Callegari, J.P. Oliveira, K. Aristizabal, R.S. Coelho, P.P. Brito, L. Wu, N. Schell, F.A. Soldera, F. Mücklich, H.C. Pinto, In-situ synchrotron radiation study of the aging response of Ti-6Al-4V alloy with different starting microstructures, Mater. Char. 165 (2020), 110400, https://doi.org/10.1016/j.matchar.2020.110400.

[8] B. Callegari, J.P. Oliveira, R.S. Coelho, P.P. Brito, N. Schell, F.A. Soldera, F. Mücklich, M.I. Sadik, J.L. García, H.C. Pinto, New insights into the micro-structural evolution of Ti-5Al-5Mo-5V-3Cr alloy during hot working, Mater. Char. 162 (2020), 110180, https://doi.org/10.1016/j.matchar.2020.110180.

[9] H.C. Lin, P.H. Tsai, I.H. Ke, J.B. Li, J. Jang, C.H. Huang, J.C. Haung, Designing a toxic-element-free Ti-based amorphous alloy with remarkable supercooled liquid region for biomedical application, Intermetallics 55 (2014) 22–27, https://doi.org/10.1016/j.intermet.2014.07.003.

[10] J.-J. Oak, A. Inoue, Attempt to develop Ti-based amorphous alloys for bio-materials, Mater. Sci. Eng., A (2007) 220–224, https://doi.org/10.1016/j.msea.2006.02.307, 449–451.

[11] S. Bera, P. Ramasamy, D. Şopu, B. Sarac, J. Zálešák, C. Gammer, M. Stoica, M. Calin, J. Eckert, Tuning the glass forming ability and mechanical properties of Ti-based bulk metallic glasses by Ga additions, J. Alloys Compd. 793 (2019) 552–563, https://doi.org/10.1016/j.jallcom.2019.04.173.

[12] S. Abdi, S. Oswald, P.F. Gostin, A. Helth, J. Sort, M.D. Baró, M. Calin, L. Schultz, J. Eckert, A. Gebert, Designing new biocompatible glass-forming Ti75-x Zr10 Nbx Si15 (x = 0, 15) alloys: corrosion, passivity, and apatite formation, J. Biomed. Mater. Res. B Appl. Biomater. 104 (2016) 27–38, https://doi.org/10.1002/jbm.b.33332.

[13] M. Zhang, Y.Q. Song, H.J. Lin, Z. Li, W. Li, A brief introduction on the devel-opment of Ti-based metallic glasses, Front. Mater. 8 (2022), 814629, https://doi.org/10.3389/fmats.2021.814629.

[14] F. Qin, Z. Dan, X. Wang, G. Xie, A. Inoue, Ti-based bulk metallic glasses for biomedical applications, in: A. Laskovski (Ed.), Biomedical Engineering, Trends in Materials Science, InTech, 2011.

[15] C.I.A. Suryanarayana, Bulk Metallic Glasses, CRC Press, [S.l.], 2020.

[16] Binary alloy phase diagrams, in: H. Okamoto, M.E. Schlesinger, E.M. Mueller (Eds.), Alloy Phase Diagrams, ASM International, 2016, p. 89.

[17] M.Q. Tang, H.F. Zhang, Z.W. Zhu, H.M. Fu, A.M. Wang, H. Li, Z.Q. Hu, TiZr-Base bulk metallic glass with over 50 mm in diameter, J. Mater. Sci. Technol. 26 (2010) 481–486, https://doi.org/10.1016/S1005-0302(10)60077-1.

[18] L. Zhang, M.Q. Tang, Z.W. Zhu, H.M. Fu, H.W. Zhang, A.M. Wang, H. Li, H.F. Zhang, Z.Q. Hu, Compressive plastic metallic glasses with exceptional glass forming ability in the Ti–Zr–Cu–Fe–Be alloy system, J. Alloys Compd. 638 (2015) 349–355, https://doi.org/10.1016/j.jallcom.2015.03.120.

[19] G. Sjögren, G. Sletten, J.E. Dahl, Cytotoxicity of dental alloys, metals, and ce-ramics assessed by millipore filter, agar overlay, and MTT tests, J. Prosthet. Dent 84 (2000) 229–236, https://doi.org/10.1067/mpr.2000.107227.

[20] W.M. Elshahawy, I. Watanabe, P. Kramer, In vitro cytotoxicity evaluation of elemental ions released from different prosthodontic materials, Dent. Mater. 25 (2009) 1551–1555, https://doi.org/10.1016/j.dental.2009.07.008.

[21] Y. Guo, I. Bataev, K. Georgarakis, A.M. Jorge, R.P. Nogueira, M. Pons, A.R. Yavari, Ni- and Cu-free Ti-based metallic glasses with potential biomedical applica-tion, Intermetallics 63 (2015) 86–96, https://doi.org/10.1016/j.intermet.2015.04.004.

[22] S. Abdi, M. Bönisch, S. Oswald, M.S. Khoshkhoo, W. Gruner, M. Lorenzetti, U. Wolff, M. Calin, J. Eckert, A. Gebert, Thermal oxidation behavior of glass-forming Ti–Zr–(Nb)–Si alloys, J. Mater. Res. 31 (2016) 1264–1274, https://doi.org/10.1557/jmr.2016.122.

[23] J.C. Hornez, A. Lefèvre, D. Joly, H.F. Hildebrand, Multiple parameter cytotox-icity index on dental alloys and pure metals, Biomol. Eng. 19 (2002) 103–117, https://doi.org/10.1016/S1389-0344(02)00017-5.

[24] A. Reyes-Jara, N. Cordero, J. Aguirre, M. Troncoso, G. Figueroa, Antibacterial effect of copper on microorganisms isolated from bovine mastitis, Front. Microbiol. 7 (2016) 626, https://doi.org/10.3389/fmicb.2016.00626.

[25] T.H. Li, P.C. Wong, S.F. Chang, P.H. Tsai, J.S.C. Jang, J.C. Huang, Biocompatibility study on Ni-free Ti-based and Zr-based bulk metallic glasses, Mater. Sci. Eng. C Mater. Biol. Appl. 75 (2017) 1–6, https://doi.org/10.1016/j.msec.2017.02.006.

[26] A. Liens, B. Ter-Ovanessian, N. Courtois, D. Fabregue, T. Wada, H. Kato, J. Chevalier, Effect of alloying elements on the microstructure and corrosion behavior of TiZr-based bulk metallic glasses, Corrosion Sci. 177 (2020), 108854, https://doi.org/10.1016/j.corsci.2020.108854.

[27] F. Qin, M. Yoshimura, X. Wang, S. Zhu, A. Kawashima, K. Asami, A. Inoue, Corrosion behavior of a Ti-based bulk metallic glass and its crystalline alloys, Mater. Trans. 48 (2007) 1855–1858, https://doi.org/10.2320/matertrans.MJ200713.

[28] S. Abdi, Investigation of New Ti-Based Metallic Glasses with Improved Me-chanical Properties and Corrosion Resistance for Implant Applications, Dres-den, Technische Universität Dresden, Diss., 2015. Dresden, 2015.

[29] M. Nicoara, A. Raduta, R. Parthiban, C. Locovei, J. Eckert, M. Stoica, Low Young's modulus Ti-based porous bulk glassy alloy without cytotoxic elements, Acta Biomater. 36 (2016) 323–331, https://doi.org/10.1016/j.actbio.2016.03.020.

[30] A. Liens, A. Etiemble, P. Rivory, S. Balvay, J.-M. Pelletier, S. Cardinal, D. Fabrègue, H. Kato, P. Steyer, T. Munhoz, J. Adrien, N. Courtois, D.J. Hartmann, J. Chevalier, On the potential of bulk metallic glasses for dental implantology: case study on Ti40Zr10Cu36Pd14, Materials 11 (2018), https://doi.org/10.3390/ma11020249.

[31] G. Xie, F. Qin, S. Zhu, A. Inoue, Ni-free Ti-based bulk metallic glass with

[32] G. Xie, H. Kanetaka, H. Kato, F. Qin, W. Wang, Porous Ti-based bulk metallic glass with excellent mechanical properties and good biocompatibility, In-termetallics 105 (2019) 153–162, https://doi.org/10.1016/j.intermet.2018.12.002.

[33] J.-J. Oak, D.V. Louzguine-Luzgin, A. Inoue, Fabrication of Ni-free Ti-based bulk-metallic glassy alloy having potential for application as biomaterial, and investigation of its mechanical properties, corrosion, and crystallization behavior, J. Mater. Res. 22 (2007) 1346–1353, https://doi.org/10.1557/jmr.2007.0154.

[34] E. Yüce, L. Zarazúa-Villalobos, B. Ter-Ovanessian, E. Sharifikolouei, Z. Najmi, F. Spieckermann, J. Eckert, B. Sarac, New-generation biocompatible Ti-based metallic glass ribbons for flexible implants, Mater. Des. 223 (2022), 111139, https://doi.org/10.1016/j.matdes.2022.111139.

[35] J.-J. Oak, A. Inoue, Formation, mechanical properties and corrosion resistance of Ti–Pd base glassy alloys, J. Non-Cryst. Solids 354 (2008) 1828–1832, https://doi.org/10.1016/j.jnoncrysol.2007.10.025.

[36] M. Nicoara, A. Raduta, C. Locovei, D. Buzdugan, M. Stoica, About thermosta-bility of biocompatible Ti–Zr–Ta–Si amorphous alloys, J. Therm. Anal. Calo-rim. 127 (2017) 107–113, https://doi.org/10.1007/s10973-016-5532-5.

[37] Y. Song, L. Peng, M. Zhang, H. Lin, S. Guo, Effects of microalloying on the isothermal and non-isothermal crystallization behaviors of TiZrSi-based metallic glasses, J. Mater. Sci. 57 (2022) 7980–7996, https://doi.org/10.1007/s10853-022-07177-w.

[38] A. Inoue, Stabilization of metallic supercooled liquid and bulk amorphous alloys, Acta Mater. 48 (2000) 279–306, https://doi.org/10.1016/S1359-6454(99)00300-6.

[39] A. Debski, R. Debski, W. Gasior, New features of entall database: comparison of experimental and model formation enthalpies/nowe funkcje bazy danych entall: porównanie doświadczalnych I modelowych entalpii tworzenia, Arch. Metall. Mater. 59 (2014) 1337–1343, https://doi.org/10.2478/amm-2014-0228.

[40] G. Ashiotis, A. Deschildre, Z. Nawaz, J.P. Wright, D. Karkoulis, F.E. Picca, J. Kieffer, The fast azimuthal integration Python library: pyFAI, J. Appl. Crys-tallogr. 48 (2015) 510–519, https://doi.org/10.1107/s1600576715004306.

[41] S. Fashu, M. Lototskyy, M.W. Davids, L. Pickering, V. Linkov, S. Tai, T. Renheng, X. Fangming, P.V. Fursikov, B.P. Tarasov, A review on crucibles for induction melting of titanium alloys, Mater. Des. 186 (2020), 108295, https://doi.org/10.1016/j.matdes.2019.108295.

[42] F.-F. Cai, B. Sarac, Z. Chen, C. Czibula, F. Spieckermann, J. Eckert, Surmounting the thermal processing limits: patterning TiZrCuPdSn bulk metallic glass even with nanocrystallization, Materials Today Advances 16 (2022), 100316, https://doi.org/10.1016/j.mtadv.2022.100316.

[43] H.Y. Jung, M. Stoica, S. Yi, D.H. Kim, J. Eckert, Electrical and magnetic prop-erties of Fe-based bulk metallic glass with minor Co and Ni addition, J. Magn. Magn Mater. 364 (2014) 80–84, https://doi.org/10.1016/j.jmmm.2014.04.028.

[44] F. Wang, A. Inoue, Y. Han, F.L. Kong, S.L. Zhu, E. Shalaan, F. Al-Marzouki, A. Obaid, Excellent soft magnetic Fe-Co-B-based amorphous alloys with extremely high saturation magnetization above 1.85 T and low coercivity below 3 A/m, J. Alloys Compd. 711 (2017) 132–142, https://doi.org/10.1016/j.jallcom.2017.03.341.

[45] O.N. Senkov, D.B. Miracle, Effect of the atomic size distribution on glass forming ability of amorphous metallic alloys, Mater. Res. Bull. 36 (2001) 2183–2198, https://doi.org/10.1016/S0025-5408(01)00715-2.

[46] M.-X. Li, Y.-T. Sun, C. Wang, L.-W. Hu, S. Sohn, J. Schroers, W.-H. Wang, Y.-H. Liu, Data-driven discovery of a universal indicator for metallic glass forming ability, Nat. Mater. (2021), https://doi.org/10.1038/s41563-021-01129-6.

[47] F.E. Luborsky (Ed.), Amorphous Metallic Alloys, Butterworths, London, 1983.

[48] H.S. Chen, Glassy metals, Rep. Prog. Phys. 43 (1980) 353–432, https://doi.org/10.1088/0034-4885/43/4/001.

[49] N. Neuber, M. Sadeghilaridjani, N. Ghodki, O. Gross, B. Adam, L. Ruschel, M. Frey, S. Muskeri, M. Blankenburg, I. Gallino, R. Busch, S. Mukherjee, Effect of composition and thermal history on deformation behavior and cluster connections in model bulk metallic glasses, Sci. Rep. 12 (2022), 17133, https://doi.org/10.1038/s41598-022-20938-6.

[50] B. Sarac, V. Zadorozhnyy, Y.P. Ivanov, F. Spieckermann, S. Klyamkin, E. Berdonosova, M. Serov, S. Kaloshkin, A.L. Greer, A.S. Sarac, J. Eckert, Tran-sition metal-based high entropy alloy microfiber electrodes: corrosion behavior and hydrogen activity, Corrosion Sci. 193 (2021), 109880, https://doi.org/10.1016/j.corsci.2021.109880.

[51] C. Liu, Q. Bi, A. Leyland, A. Matthews, An electrochemical impedance spec-troscopy study of the corrosion behaviour of PVD coated steels in 0.5 N NaCl aqueous solution: Part II, Corrosion Sci. 45 (2003) 1257–1273, https://doi.org/10.1016/S0010-938X(02)00214-7.

[52] M.R. Shoar Abouzari, F. Berkemeier, G. Schmitz, D. Wilmer, On the physical interpretation of constant phase elements, Solid State Ionics 180 (2009) 922–927, https://doi.org/10.1016/j.ssi.2009.04.002.

[53] C.H. Hsu, F. Mansfeld, Technical Note: Concerning the Conversion of the Constant Phase Element Parameter Y0 into a Capacitance, 57, Corrosion, 2001.

[54] X. Lyu, W.-N. Zhang, W. Li, B.-W. Shi, Y.-N. Zhang, H. Chen, S.-C. Li, X. Wang, Two-dimensional porous PtPd nanostructure electrocatalysts for oxygen reduction reaction, ACS Appl. Nano Mater. 3 (2020) 8586–8591, https://

doi.org/10.1021/acsanm.0c01900.

[55] Q. Zhang, T. Shao, Y. Li, D. Bai, Z. Xue, S. He, D. Zhang, X. Zhou, One-step fabrication of bimetallic PtPd mesoporous nanospheres for methanol electrooxidation, J. Electroanal. Chem. 911 (2022), 116197, https://doi.org/10.1016/j.jelechem.2022.116197.

[56] Y. Lu, Y. Jiang, W. Chen, PtPd porous nanorods with enhanced electrocatalytic activity and durability for oxygen reduction reaction, Nano Energy 2 (2013) 836–844, https://doi.org/10.1016/j.nanoen.2013.02.006.

[57] Z. Liu, Y. Li, X. Zhang, S. Rao, J. Li, W. Wang, Z. Sun, J. Yang, Surface structure engineering of PtPd nanoparticles for boosting ammonia oxidation electrocatalysis, ACS Appl. Mater. Interfaces 14 (2022) 28816–28825, https://doi.org/10.1021/acsami.2c04711.

[58] Y.Y. Rivera-Lugo, K.I. Pérez-Muñoz, B. Trujillo-Navarrete, C. Silva-Carrillo, E.A. Reynoso-Soto, J.C. Calva Yañez, S.W. Lin, J.R. Flores-Hernández, R.M. Félix-Navarro, PtPd hybrid composite catalysts as cathodes for proton exchange membrane fuel cells, Energies 13 (2020) 316, https://doi.org/10.3390/en13020316.